

## Article

# Crystal Structure and XPS Study of Titanium-Substituted M-Type Hexaferrite BaFe<sub>12-x</sub>Ti<sub>x</sub>O<sub>19</sub>

Kim-Isabelle Mehnert <sup>1,2</sup>, Manuel Häßner <sup>1</sup>, Yanina Mariella Dreer <sup>1</sup>, Indro Biswas <sup>2</sup> and Rainer Niewa <sup>1,\*</sup><sup>1</sup> Institute of Inorganic Chemistry, University of Stuttgart, Pfaffenwaldring 55, 70569 Stuttgart, Germany<sup>2</sup> Institute of Engineering Thermodynamics, German Aerospace Center (DLR), Pfaffenwaldring 38-40, 70569 Stuttgart, Germany; indro.biswas@dlr.de

\* Correspondence: rainer.niewa@iac.uni-stuttgart.de

**Abstract:** The M-type barium hexaferrite substituted with titanium, BaFe<sub>12-x</sub>Ti<sub>x</sub>O<sub>19</sub>, was synthesized from sodium carbonate flux and the obtained single crystals with a maximum degree of substitution of up to about  $x = 0.9$  were characterized. XPS measurements were carried out for the identification of side products and in particular in order to assign the valence states of the transition-metal constituents. Due to the aliovalent exchange of iron(III) with titanium(IV), an additional charge balance needs to occur. No titanium(III) was detected, while the amount of iron(II) increased in the same order of magnitude as the amount of titanium(IV); thus, the major charge balancing is attributed to the reduction of iron(III) to iron(II). According to the XPS data, the amount of titanium(IV) typically is slightly higher than that of iron(II). This is in line with a tendency to a minor formation of vacancies on the transition-metal sites becoming more important at higher substitution levels according to PXRD and WDS measurements, completing the picture of the charge-balance mechanism. XRD taken on single crystals indicates the distribution of titanium and vacancies over three of the five transition-metal sites.

**Keywords:** ferrites; flux crystal growth; XRD; SEM; WDS; XPS

**Citation:** Mehnert, K.-I.; Häßner, M.; Dreer, Y.M.; Biswas, I.; Niewa, R. Crystal Structure and XPS Study of Titanium-Substituted M-Type Hexaferrite BaFe<sub>12-x</sub>Ti<sub>x</sub>O<sub>19</sub>. *Inorganics* **2023**, *11*, 207. <https://doi.org/10.3390/inorganics11050207>

Academic Editor: Vincent Harris

Received: 24 March 2023

Revised: 19 April 2023

Accepted: 28 April 2023

Published: 10 May 2023



**Copyright:** © 2023 by the authors. Licensee MDPI, Basel, Switzerland. This article is an open access article distributed under the terms and conditions of the Creative Commons Attribution (CC BY) license (<https://creativecommons.org/licenses/by/4.0/>).

## 1. Introduction

Ferrites are magnetic ceramics with iron in oxidation state +III as their basis. The most common composition is the M-type BaFe<sub>12</sub>O<sub>19</sub>, also known as hexaferrite, barium ferrite or ferroxdure. Hexaferrites are used in an enormously large area of applications for energy transformation, for example for the inductive charging of batteries, motors, transport, security, diagnostic devices, computers and communication devices, to name only a few [1–3]. As of 2012, a total of 3012 patents regarding hexagonal ferrites are registered and most ferrimagnetic ceramics are made of them [1]. In 1938 the structure of BaFe<sub>12</sub>O<sub>19</sub> was solved by Adelsköld [4], crystallizing in a hexagonal crystal lattice with  $a = 588.8(3)$  pm and  $c = 2316.8(3)$  pm, space group  $P6_3/mmc$  and with two formula units in the unit cell,  $Z = 2$  [5]. By adding defined amounts of other cations the iron can be partly substituted while retaining the M-type structure. Furthermore, other types with differing structures and compositions can be obtained, where until today new types are discovered [6,7]. Aliovalent substitution of iron(III) by tetravalent titanium in the M-type ferrite was reported [8–16], where the structure could be retained to a limited extent [8]. Questioning the charge-balance mechanisms reveals that valence-state assignments are not always straightforward, as substitution with manganese shows [17]. The exact mechanism for charge balance in the system with titanium substituting iron is not completely understood until today. Generally speaking, titanium(IV) can substitute iron(III) either while forming vacancies in the metal substructure (1/3 iron(III) per introduced titanium(IV)) or via the reduction of iron(III) to iron(II) or of titanium(IV) to titanium(III) [8,9,18].

<sup>57</sup>Fe-Mössbauer spectroscopy at unsubstituted and titanium(IV) substituted M-type ferrites reveals the presence of six, seven or eight superimposed sextets and one or two

doublets. Taking the entire literature together, every iron site was discussed as the preferred one for substitution with titanium at least once [9,12,14–16].

In the present work, crystals of M-type hexaferrites substituted with titanium(IV) in the range of  $0 \leq x \leq 1$  within the composition  $\text{BaFe}_{12-x}\text{Ti}_x\text{O}_{19}$  were grown from sodium carbonate flux. The compositions of the obtained crystals were determined with energy and wavelength dispersive X-ray spectroscopy (EDS and WDS). Characterization with a combination of X-ray diffraction on powders and single crystals (PXRD and SCXRD) and visualization with scanning electron microscopy (SEM) contributes to the elucidation of the structure. X-ray photoelectron spectroscopy (XPS) was performed in order to identify the side products and residues from synthesis at the surface and particularly to determine the valence states of titanium and iron. Taking all results together reveals a more complete picture of the distribution of titanium over the various crystallographic sites and the charge-balancing mechanism for the aliovalent substitution of iron(III) by titanium(IV) within this hexaferrite system. These general results can be transferred to various substituted ferrite systems and aid the directed synthesis of single-phase samples with specific degrees of substitution including co-substituted materials.

## 2. Results and Discussion

The quaternary system Ba–Fe–Ti–O is very rich in phases and well investigated [19]. In the present work the impact of different oxidation states of iron and titanium on the structure and system shall be investigated. We were able to grow single crystals of  $\text{BaFe}_{12-x}\text{Ti}_x\text{O}_{19}$  with different degrees of substitution  $x$  determined to be in the range between 0.1 and 1. Additionally, one unsubstituted M-type ferrite  $\text{BaFe}_{12}\text{O}_{19}$  was synthesized for reference and studied as well (degree of substitution  $x = 0$ ). The compositions of the individual crystals were determined with WDS measurements. The resulting amount of vacancies on transition-metal sites effective for charge balancing was calculated. The exact composition of the studied crystals according to WDS can be found in Table 1. Based on the results from SCXRD, the structure and possible sites for titanium are discussed. With WDS and PXRD measurements the nominal degree of substitution from synthesis  $x_{\text{nom}}$  and the actual measured degree of substitution  $x_{\text{WDS}}$  are compared and the influence on the unit cell parameters is discussed. The valence states of iron and titanium are determined with XPS measurements at five single crystals. These particular crystals were additionally measured with WDS and the three most suitable out of five with SCXRD were determined. Taking all the results together, the possible mechanisms for charge balance involving vacancies are discussed.

### 2.1. Composition Determination with WDS

WDS measurements were performed on all the single crystals discussed in this work, applying various standard materials for higher accuracy, in order to determine the compositions and prove the absence of significant composition gradients. As the quantification of light elements such as oxygen with WDS is prone to large errors, its values were calculated assuming  $\text{Ba}^{2+}$ ,  $\text{Fe}^{3+}$  and  $\text{Ti}^{4+}$ , thus slightly overestimating the oxygen content in case of the presence of minor  $\text{Fe}^{2+}$  contributions. The results for the calculated compositions can be found in Table 1 and the corresponding measurement data are listed in Tables S1–S3 in the Supplementary Materials.

In addition, SEM images of the crystals were taken to facilitate the selection of suitable measuring points and to identify any impurities that may be present on the crystal surface. An exemplary SEM picture of the surface of an investigated single crystal is given in Figure 1 and additional images can be found in Figures S1–S9 in the Supplementary Materials.

Now, analyzing the measured WDS data, possible vacancies in the structure for charge balancing should be considered as well. The resulting amounts of titanium and iron in the compositions are summed up and subtracted from 12, being the amount of transition metal in the ideal hexaferrite composition. The resulting number  $y$  is considered the vacancy concentration and symbolized with a square  $\square$ ; the composition derived from WDS data is

given as  $\text{BaFe}_{12-x-y}\text{Ti}_x\text{O}_{19}$ . The nominal degree of substitution according to synthesis  $x_{\text{nom}}$  and according to WDS  $x_{\text{WDS}}$  and the compositions according to SCXRD and WDS are listed in Table 1. These five single crystals were additionally investigated with XPS, regarding their Fe(II)/Fe(III) ratio. The composition according to SCXRD will be discussed in detail in Section 2.2 and the WDS measurement data can be found in Table S1 in the Supplementary Materials.

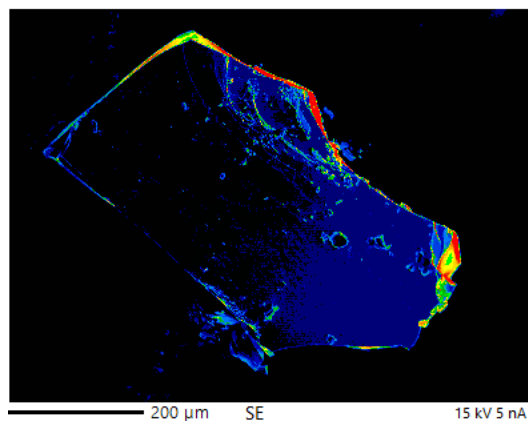


**Figure 1.** Exemplary SEM picture of an investigated single crystal with composition  $\text{BaFe}_{10.7(2)}\text{Ti}_{0.91(7)}\square_{0.36}\text{O}_{19}$ . The  $\square$  symbolizes a vacancy on the transition-metal sites. The number of secondary electrons detected is increasing from blue to green to red, as the crystal edges are facing towards the off-axis detector.

**Table 1.** Degrees of substitution  $x$  in  $\text{BaFe}_{12-x-y}\text{Ti}_x\text{O}_{19}$  from synthesis  $x_{\text{nom}}$  and WDS measurements  $x_{\text{WDS}}$ , as well as the compositions according to SCXRD and WDS measurements. Compositions SCXRD and WDS in one line were obtained from the identical crystal.

$x_{\text{nom}}$	Composition SCXRD	$x_{\text{WDS}}$	Composition WDS
0.0	$\text{BaFe}_{12}\text{O}_{19}$	0	$\text{BaFe}_{11.98(19)}\square_{0.02}\text{O}_{19}$
0.1	–	0.143(5)	$\text{BaFe}_{11.81(18)}\text{Ti}_{0.143(5)}\square_{0.05}\text{O}_{19}$
1.1	–	0.49(1)	$\text{BaFe}_{11.39(18)}\text{Ti}_{0.49(1)}\square_{0.12}\text{O}_{19}$
0.7	$\text{BaFe}_{11.3(2)}\text{Ti}_{0.7(2)}\text{O}_{19}$	0.65(3)	$\text{BaFe}_{11.11(23)}\text{Ti}_{0.65(3)}\square_{0.20}\text{O}_{19}$
3.6	$\text{BaFe}_{9.0(4)}\text{Ti}_{3.0(4)}\text{O}_{19}$	0.91(7)	$\text{BaFe}_{10.73(19)}\text{Ti}_{0.91(7)}\square_{0.36}\text{O}_{19}$

Due to a high amount of iron in the structure, its error margin is as large as the calculated amount of vacancies. Consequently, the calculated small but significant amount of vacancies should be considered with care.

For example, a crystal with the composition  $\text{BaFe}_{10.7(2)}\text{Ti}_{0.91(7)}\square_{0.36}\text{O}_{19}$  according to WDS was scanned and the elements barium, iron and titanium were quantified. The results are visualized in Figure 2.

An apparent slight compositional gradient is due to the fact that the crystal surface is not perfectly orthogonally orientated to the electron beam rather than to a real gradient. Thus, a homogeneous distribution of the metallic constituents is revealed. Because of WDS being a surface-analysis method, a gradient of composition within the interior of the crystal cannot be detected.

## 2.2. Crystal Structure from SCXRD

The crystal structures of the crystals with different titanium contents were determined via SCXRD. All investigated crystals share the structure type of the unsubstituted magnetoplumbite  $\text{PbFe}_{12}\text{O}_{19}$  [20]. The crystallographic data and measurement conditions, Wyckoff-sites, fractional coordinates in the asymmetric unit, occupational parameters as well as isotropic displacement parameters for every unique site are listed in Tables S4–S15 in the Supplementary Materials.

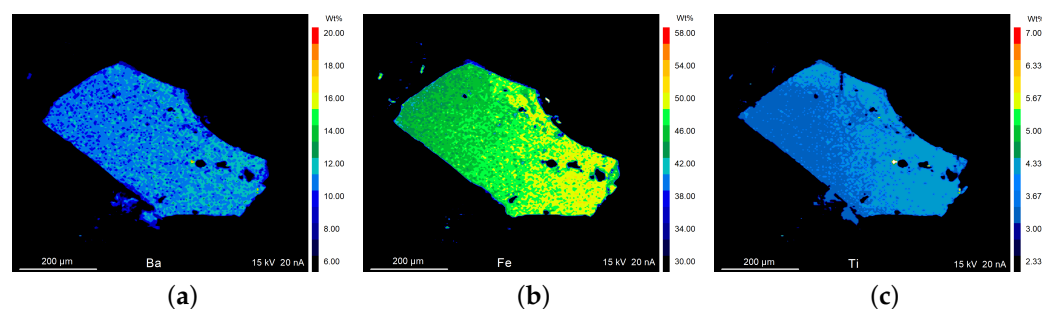


**Figure 2.** Quantitative results for elemental distribution obtained from WDS scan on a single crystal  $\text{BaFe}_{10.7(2)}\text{Ti}_{0.91(7)}\square_{0.36}\text{O}_{19}$  for (a) barium, (b) iron and (c) titanium.

In the refinements, a mixed occupation with iron and titanium on the fully occupied transition-metal sites is modelled, as is found regularly for the unsubstituted  $\text{BaFe}_{12}\text{O}_{19}$ . Consequently, the refinements of the SCXRD data yield a composition with the presence of iron(III), iron(II) and titanium(IV) in the compound for achieving electroneutrality, assuming the absence of reduced titanium ions. Due to the high reaction temperature a reduction of iron(III) is more probable than a reduction of titanium(IV) [10,21]. Unfortunately, due to methodical constraints it is not possible to refine a third element or a vacancy on the sites without further constraints based on external information, since no unique solution for the occupation factors can be generated [22,23]. Thus, the presence of a significant contribution of vacancies (i.e., no electron density at the specific position) would lead to a too-low electron density and result in an overestimation of the titanium amount with fewer electrons than iron.

In general, the M-type structure consists of hexagonal and cubic close-packed layers of oxide anions and alkaline earth metal (here barium) cations with metal ions in tetrahedral, trigonal bipyramidal and octahedral voids. These layers can be combined to different blocks, whose sequence reflects the stacking order. The block-stacking sequence of M-type ferrites is  $\text{SRS}^*\text{R}^*$ , with \* indicating a rotation of the block around the *c*-axis by  $180^\circ$ . An expanded unit cell of  $\text{BaFe}_{10.7(3)}\text{Ti}_{1.3(3)}\text{O}_{19}$  with labeled blocks can be seen in Figure 3, and its SCXRD measurement data are listed in Tables S13–S15 in the Supplementary Materials.

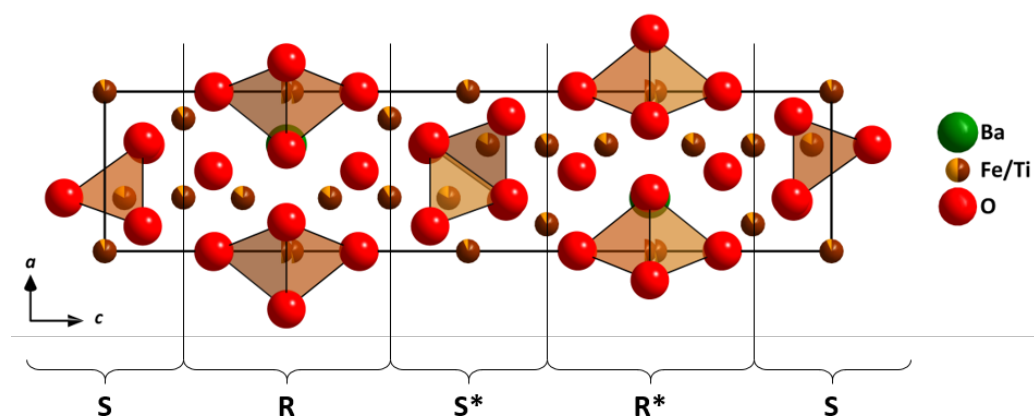


**Figure 3.** Expanded unit cell of  $\text{BaFe}_{10.7(3)}\text{Ti}_{1.3(3)}\text{O}_{19}$  with labeled blocks. The coordination polyhedra of tetrahedral and trigonal bipyramidal coordinated metal sites are shown as well.

The metal ions of M-type ferrites occupy six crystallographically different Wyckoff sites. Barium, which replaces one-fourth of the oxygen ions of the oxide layer in the middle of the R-block, occupies the Wyckoff site  $2d$  and is surrounded anticuboctahedrally by oxide anions. Furthermore, the R-block contains the trigonal bipyramidal coordinated  $M(2)$  (Wyckoff site  $4e$ ) and the octahedrally coordinated  $M(4)$  (Wyckoff site  $4f$ ), where  $M$  is a transition-metal ion. The S-block comprises the octahedrally coordinated  $M(1)$  ions on Wyckoff site  $2a$  and the tetrahedrally coordinated  $M(3)$  (Wyckoff site  $4f$ ). The octahedrally

coordinated  $M(5)$  ions (Wyckoff site  $12k$ ) form a kagome network, which connects the R- and S-blocks. The coordination polyhedra of the metal ions are shown in Figure 4. The cations with their corresponding Wyckoff sites, coordination numbers and R/S-block affiliation are also listed in Table 2.

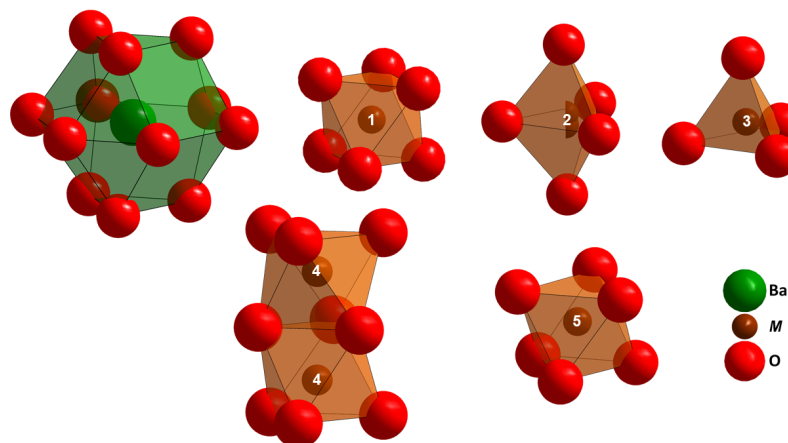


**Figure 4.** Coordination polyhedra of barium (green) and the transition-metal sites  $M(1)$ – $M(5)$  (red).

**Table 2.** Coordination numbers (CN), Wyckoff sites and corresponding block locations of metal ions within the hexaferrite crystal structure.

Atom	Wyckoff Site	CN	Block Location
Ba	$2d$	12	R
$M(1)$	$2a$	6	S
$M(2)$ <sup>a</sup>	$4e$	5	R
$M(3)$	$4f$	4	S
$M(4)$	$4f$	6	R
$M(5)$	$12k$	6	R/S

<sup>a</sup> occupation factor 50%.

In the refinements of the titanium-substituted crystals sites,  $M(1)$  and  $M(2)$ , located in octahedral and trigonal bipyramidal coordination by oxygen, result in a low occupation for titanium with a relatively high error margin. For most investigated substituted crystals, it was not even possible to refine these positions partially occupied with iron and titanium. Apparently, these sites are unaffected by substitution with titanium and no significant tendency for formation of vacancies appears. In other words, within the accuracy of the method, these two sites seem always fully occupied with iron.

The transition-metal sites  $M(3)$ ,  $M(4)$  and  $M(5)$  with tetrahedral and two-times octahedral coordination, respectively, are preferred for titanium substitution according to the SCXRD results, since the amount of titanium in the refinement results is higher and the error margins are lower at these sites. However, as indicated above, vacancy formation at these sites might mimic a too-high titanium-to-iron ratio. Two  $M(4)$  cations occupy two face-sharing octahedra of the surrounding oxide anions. Consequently, the mutual distance between the transition-metal atoms  $M(4)$  in the centers of these octahedra is shorter compared to all other distances between transition-metal atoms in the structure. To counteract this situation, the transition-metal atoms at site  $M(4)$  are slightly deflected from the centres of the octahedra, resulting in a slightly enlarged distance of about 280 pm, but still 15–25 pm shorter compared to the mutual distances of  $M(5)$  situated in the edge-sharing polyhedra forming the kagome lattice. According to Pauling's rules, these  $M(4)$  sites should not be favored for highly charged cations [24].

Mariño-Castellanos et al. published a phenomenological model for predicting the distribution of substituted cations among iron sites in 2011 [11]. Applying this model leads

to the assumption that titanium favors octahedral sites ( $M(1)$ ,  $M(4)$  and  $M(5)$ ), which is in agreement with our results from SCXRD for  $M(4)$  and  $M(5)$ . However, it disagrees with the high occupation of  $M(3)$  by titanium in the structure refinements and the fact that no occupation of  $M(1)$  is found in this diffraction study.

Concerning mechanisms for electroneutrality, it is more probable that the face-sharing pair of octahedra ( $M(4)$ ) is filled with one titanium(IV) and one iron(II) or a vacancy in the other. The first possibility can also be observed in Ilmenite  $\text{FeTiO}_3$  [25,26].

### 2.3. Nominal vs. Actual Degree of Substitution and Influence on Unit Cell Parameters

For statistical purposes, from each sample three larger single crystals with an edge length of 0.3–1.0 mm and a smooth surface were selected and 6–24 points were investigated with WDS at each. Due to poorly developed crystal growth and multi-phase samples at a higher nominal degree of substitution  $x_{\text{nom}}$ , only one single crystal could be selected for these. The results are graphically depicted in Figure 5 and the corresponding WDS data can be found in Tables S2 and S3 in the Supplementary Materials.

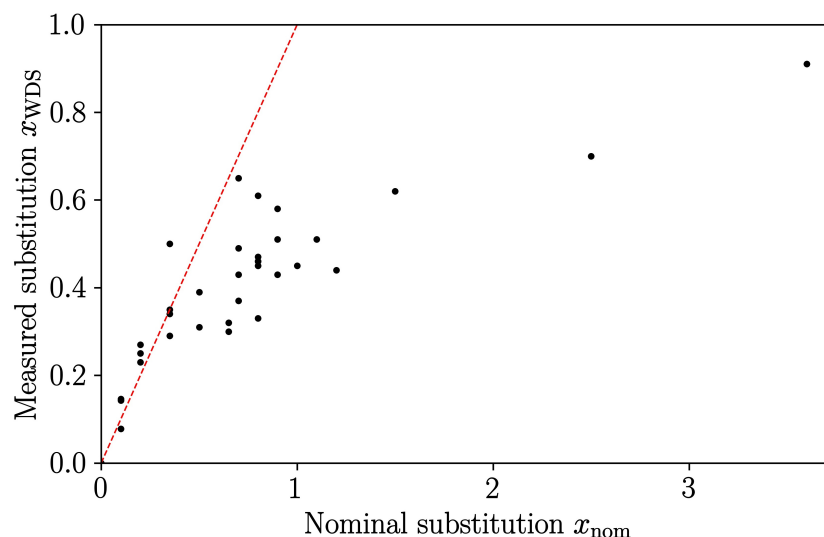


**Figure 5.** Degree of substitution according to WDS  $x_{\text{WDS}}$  plotted against nominal degree of substitution from synthesis  $x_{\text{nom}}$ . The dashed red line symbolizes the trend if full incorporation of titanium into the ferrite during synthesis were to occur.

Starting with a nominal degree of substitution  $x_{\text{nom}} = 0.35$ , according to the WDS measurements, the actual amount of titanium in the structure is not proportional anymore. For these samples with increased  $x_{\text{nom}}$ , less titanium than expected for full incorporation during synthesis is included in the ferrite crystals and more side-products, e.g.,  $\text{BaTiO}_3$ ,  $\text{FeTiO}_3$  and  $\text{NaFeTiO}_4$ , are generated.

From twelve synthesis experiments with different nominal degrees of substitution  $x_{\text{nom}}$  several single crystals were selected and investigated with WDS. For each experiment, an arithmetic average  $\bar{x}_{\text{WDS}}$  was calculated from the individual  $x_{\text{WDS}}$ . The corresponding data can be found in Table S2 in the Supplementary Materials. For each of the samples, a phase analysis via PXRD was rendered. One of the resulting patterns is shown as an example in Figure 6, while the remaining patterns can be found in Figures S10–S21 in the Supplementary Materials.

Le Bail fits were performed for determining the unit cell parameters  $a$  and  $c$  and calculating the unit cell volume  $V$ . Finally,  $a$ ,  $c$  and  $V$  are plotted against the arithmetic average  $\bar{x}_{\text{WDS}}$  in Figure 7.

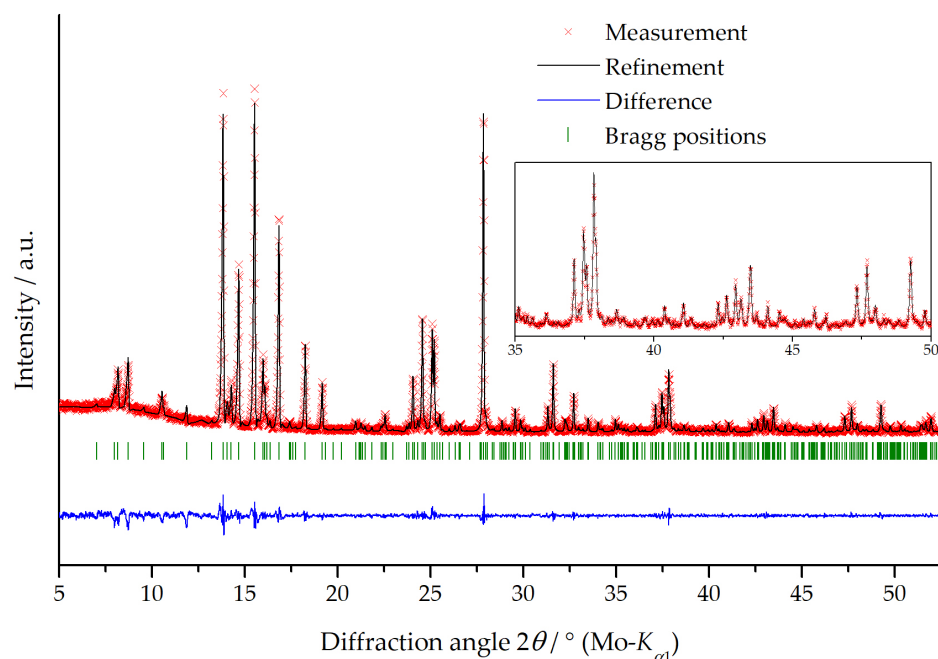


**Figure 6.** PXRD measurement (red) of nominal BaFe<sub>11.90</sub>Ti<sub>0.10</sub>O<sub>19</sub> with Le Bail fit (black) for calculating unit cell parameters  $a$  and  $c$ , difference curve (blue) and Bragg positions (green). Inset: Enlarged range from 35° to 50°.

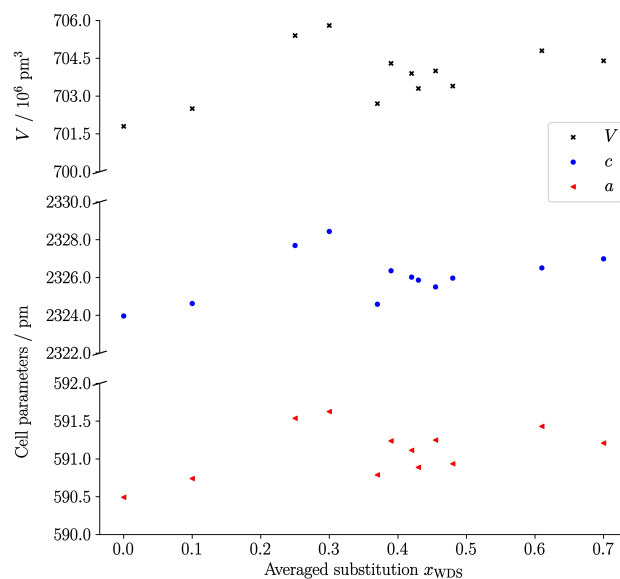


**Figure 7.** Unit cell parameters  $a$  (red triangles) and  $c$  (blue circles) from Le Bail profile refinement and calculated unit cell volume  $V$  (black crosses) plotted against degree of substitution from WDS  $x_{WDS}$ .

Initially,  $a$  and  $c$  increase monotonically with a rising amount of titanium(IV) up to  $x_{WDS} \approx 0.3$ . For higher  $x_{WDS}$  a drop in the cell parameters is observed, followed by a slight increase. Additionally, the values for samples with  $x_{WDS} > 0.3$  reveal substantial scattering.

According to Shannon, the effective ionic radius of a high-spin Fe<sup>3+</sup> ion in six-fold coordination equals 64.5 pm, high-spin Fe<sup>2+</sup> in six-fold coordination 77.7 pm and Ti<sup>4+</sup> in six-fold coordination 60.5 pm [27]. Assuming the substitution of iron(III) by the smaller titanium(IV) and concomitant formation of a significant degree of vacancies would result in an expected reduction in the unit cell volume. On the contrary, the reduction of iron(III) to larger iron(II) for charge balancing the titanium(IV) incorporation should provoke an increased unit cell. Based on the observed dependence of the unit cell parameters on the

average titanium content, we speculate a dominating reduction of iron(III) to iron(II) up to  $x_{\text{WDS}} \approx 0.3$  being responsible for the initial increase. However, at higher degrees of substitution the formation of vacancies add to the further reduction of iron(III), thus leading to the monitored inexplicit trend in Figure 7.

#### 2.4. Valence States from XPS

Five titanium substituted M-type ferrite crystals with degrees of substitution  $0 \leq x < 1$  according to WDS, as listed in Table 1, were additionally investigated with XPS. If possible, for statistical purposes several points were chosen at the surface of one crystal for measurement, data fitted and atomic ratios calculated. The qualitative analysis of the XPS spectra was performed with help of the database by Moulder et al. [28]. For example, an XPS survey spectrum of  $\text{BaFe}_{10.73(19)}\text{Ti}_{0.91(7)}\text{O}_{19}$  is shown in Figure 8. Among the five overview spectra of the studied samples, the presented graph shows the highest titanium signal ( $\sim 458$  eV) due to the highest degree of substitution present. In the Supplementary Materials all recorded survey spectra are shown in Figures S22–S32. In Table 3 all discussed measured binding energies and the corresponding literature are listed.

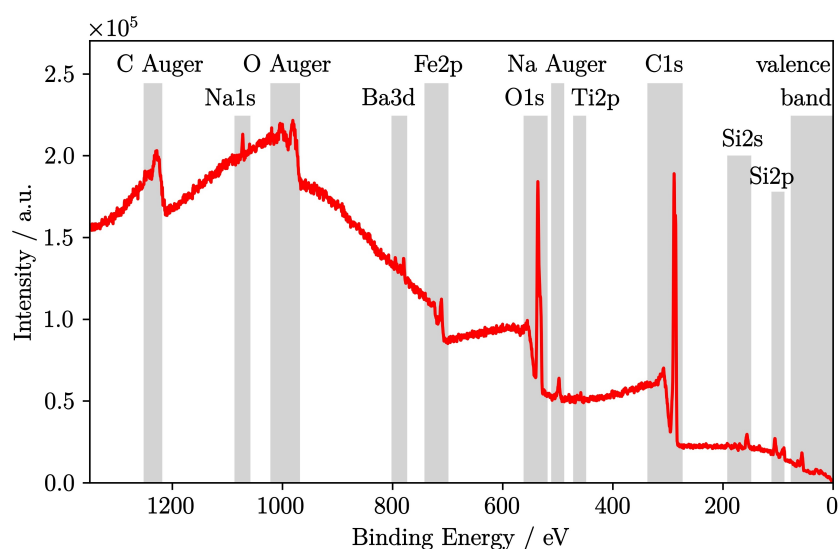


**Figure 8.** XPS survey spectrum of  $\text{BaFe}_{10.73(19)}\text{Ti}_{0.91(7)}\text{O}_{19}$ .

**Table 3.** Measured binding energies BE with corresponding values from the literature.

Signal	Measured BE/eV	BE in Lit./eV	Lit.
Si 2p (in $\text{SiO}_2$ )	103	103.3	[28]
C 1s	286	284.5	[28]
Ti(IV) 2p	458.4	458	[29]
Ti(III) 2p	—	456.6	[29]
O 1s (in ferrite)	530	529.6	[30]
O 1s (in $\text{CO}_3^{2-}$ )	532.5	531	[31]
O 1s (contamination) <sup>1</sup>	533–540	531.1/532.65	[32,33]
Fe(III) 2p (in ferrite)	710.8	710.4	[30]
Fe(III) 2p (in $\text{Fe}_2\text{O}_3$ ) <sup>2</sup>	—	710.8	[34]
Fe(II) 2p (in ferrite)	709.6	—	—
Fe(II) (in FeO)	—	709.7	[34]
Ba 3d (in ferrite)	779.3	779.3	[30]
Ba 3d (in $\text{BaCO}_3$ )	780.8	779.4	[30,35]
Na 1s	1072	1072.1	[28]

<sup>1</sup> Contamination with adsorbed air, water and partly charged particles such as silica [32,33]. <sup>2</sup> Average of recorded BEs of various  $\text{Fe}_2\text{O}_3$  modifications [34].

According to the XPS measurements, every crystal contains barium, iron and oxygen, as expected for an M-type ferrite. Crystals with a non-zero substitution level also showed signals for titanium. In addition, sodium, carbon and silicon were observed. The major carbon signal results from the fixation of the crystals on a conductive carbon-based tape.

The silicon traces on the surface of the sample are a residue of glass capillaries from the SCXRD measurements. Sodium is detected in small amounts as a residue from the fluxing agent sodium carbonate  $\text{Na}_2\text{CO}_3$  from synthesis. In the following, exemplary spectra of narrow spectral regions are shown for the composition  $\text{BaFe}_{11.18(18)}\text{Ti}_{0.62(1)}\text{O}_{19}$ . In the Supplementary Materials all measured narrow spectral regions are shown in Figures S33–S105. Figure 9 depicts the narrow spectral regions of O 1s and Ba 3d for this crystal, recorded at 30 eV pass energy.

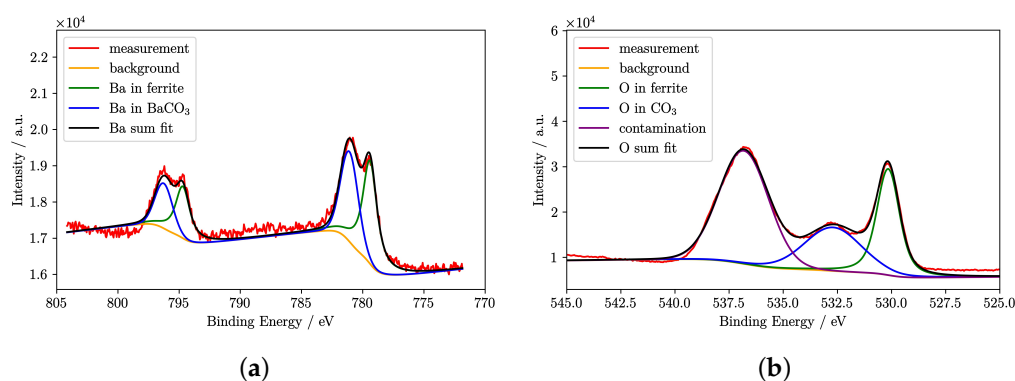


**Figure 9.** XPS spectra of  $\text{BaFe}_{11.18(18)}\text{Ti}_{0.62(1)}\text{O}_{19}$  (a) O 1s (3 signal components) (b) Ba 3d spectrum (2 doublet signal components), both including signal deconvolutions.

Between 545 and 525 eV oxygen 1s electrons show several signals, all charged electrically and thus shifted to slightly higher binding energies. The oxygen signal at 530 eV is related to the ferrite [30], at 532.5 eV oxygen is present in carbonate [31] and above 533 eV it is a signal from contaminations with adsorbed air, water and partly charged particles such as silica [32,33].

Nitrogen was not detected in the survey photoemission spectra (binding energy: 400 eV); thus, there is no evidence for remaining nitrates from washing the product. Barium 3d electrons cause two doublets at 779/795 eV in the ferrite [30] and at 780.8/796 eV, resembling barium carbonate [30,35]. Without further refinement of the secondary electron baseline, the two different Ba species can be identified and separated. The result fits well with the observed carbonate component of the oxygen signal. Thus, it can be concluded that traces of the reactant  $\text{BaCO}_3$  are present at the surface, and only the indicated ferrite Ba doublet (779/795 eV) is used for calculating the ferrite composition.

The narrow spectral region of Ti 2p is shown in Figure 10 and for Fe 2p in Figure 11. The Ti  $2p_{3/2}$  signal and the Fe  $2p_{3/2}$  were recorded additionally at 20 eV pass energy for better resolution.

Only one doublet signal of titanium(IV) at 458/464 eV binding energy was detected. For titanium(III), a doublet signal at 456/462 eV binding energy would be expected [29], but was not observed even as a trace. Due to the low signal level and, thus, a high signal-to-noise ratio the quantification of the titanium signal and subsequent calculation of ratios leads to considerable error margins (see Figure 12). With an increasing degree of substitution, as expected, the amount of titanium found in XPS increases as well.

The detailed Fe  $2p_{3/2}$  photoemission signals at  $\sim 710$  eV were used for the quantification of the Fe(II) and Fe(III) ratio. The asymmetric shape and an additional spin multiplet satellite is typical for the Fe 2p XPS signal [28]. In this work, it is assumed that in unsubstituted M-type ferrite only iron(III) is present. Thus, the signal with a binding energy of 710.8/724.1 eV is assigned to iron(III) [30,34]. The signal was fitted with two doublet signals and one satellite doublet signal; the determined parameters for iron(III) are used as a reference dataset for fitting all other Fe 2p spectra of substituted ferrites. Since the electrons of iron(II) are measured at a lower binding energy than iron(III) [34], the doublet signal at 709.6/723.0 eV is assigned to iron(II). This signal starts to appear with the substi-

tution of iron(III) by titanium(IV) and rises with an increasing amount of titanium(IV) in  $\text{BaFe}_{12-x}\text{Ti}_x\text{O}_{19}$ .

From the fitted signals the integrals were calculated. With the integrals, cross sections from J.J. Yeh and I. Lindau [36] and transmission functions from Avantage software [37] the ratios of iron(III), iron(II) and titanium(IV) were calculated and the results are listed in Tables S16–S21 in the Supplementary Materials. The arithmetic average of all points was calculated for determining the final ratios. From these, the compositions were determined as well. The results are listed in Table 4 and the ratios are plotted in Figure 12.

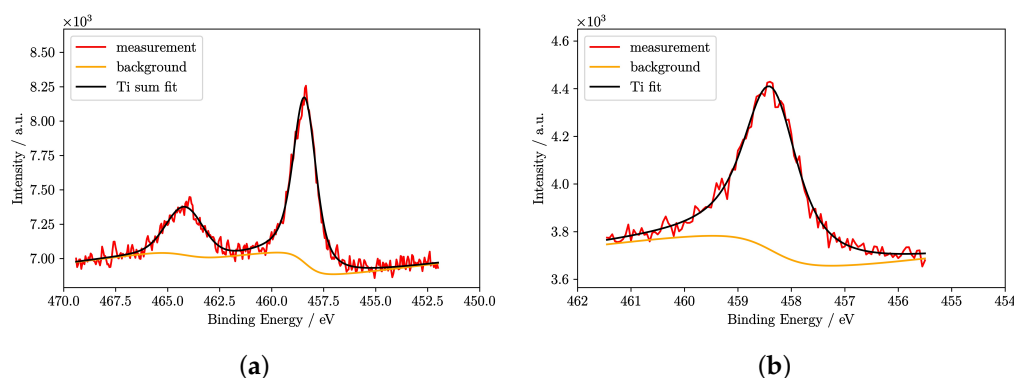


**Figure 10.** XPS Ti 2p spectra of  $\text{BaFe}_{11.18(18)}\text{Ti}_{0.62(1)}\text{O}_{19}$  (a) recorded at pass energy 30 eV (1 doublet signal) (b) detailed  $\text{Ti } 2p_{3/2}$  signal recorded at pass energy 20 eV shows no Ti(III) shoulder, both spectra including signal deconvolutions.

The error margins are noticeably higher for measurements with pass energy 30 eV, leading to more reliable results with the lower pass energy. With an increasing degree of substitution, according to the WDS measurements  $x_{\text{WDS}}$ , the amount of iron(III) is decreasing and the amount of iron(II) and titanium(IV) are increasing and always in the same order of magnitude. We can conclude that for all measured crystals major charge balancing is achieved by the reduction of iron(III) to iron(II). Due to the high error margins, the ratio of reduction of iron(III) and vacancies in the crystal lattice to compensate for the change in charge cannot be calculated. Furthermore, the differences in degrees of substitution calculated from the WDS and XPS measurement results are not discussed due to the noticeably high error margins for the titanium amount from the XPS measurements and the difference in surface sensitivity of the two techniques.

**Table 4.** Degree of substitution from WDS measurements  $x_{\text{WDS}}$ , ratio of Fe(III)/Fe(II)/Ti(IV) in % with statistical error in brackets determined with XPS measurements with pass energies 20 eV or 30 eV, respectively, and the resulting chemical formulae.

$x_{\text{WDS}}$	30 eV Pass Energy		20 eV Pass Energy	
	Fe(III)/Fe(II)/Ti(IV)/%	Composition	Fe(III)/Fe(II)/Ti(IV)/%	Composition
0	100/0/0	$\text{BaFe}_{12}^{\text{III}}\text{O}_{19}$	100/0/0	$\text{BaFe}_{12}^{\text{III}}\text{O}_{19}$
0.143(5)	86(21)/10(18)/4(4)	$\text{BaFe}_{10.3(2.5)}^{\text{III}}\text{Fe}_{1.2(2.2)}^{\text{II}}\text{Ti}_{0.5(5)}^{\text{IV}}\text{O}_{19}$	94(10)/4(8)/2(2)	$\text{BaFe}_{11.3(1.2)}^{\text{III}}\text{Fe}_{0.5(9)}^{\text{II}}\text{Ti}_{0.2(2)}^{\text{IV}}\text{O}_{19}$
0.49(1)	82(5)/7(1)/11(5)	$\text{BaFe}_{9.9(8)}^{\text{III}}\text{Fe}_{0.8(1)}^{\text{II}}\text{Ti}_{1.3(6)}^{\text{IV}}\text{O}_{19}$	82(7)/6(1)/12(7)	$\text{BaFe}_{9.9(8)}^{\text{III}}\text{Fe}_{0.7(1)}^{\text{II}}\text{Ti}_{1.4(8)}^{\text{IV}}\text{O}_{19}$
0.62(1)	71(25)/16(16)/13(14)	$\text{BaFe}_{8.5(3.0)}^{\text{III}}\text{Fe}_{1.9(1.9)}^{\text{II}}\text{Ti}_{1.6(1.7)}^{\text{IV}}\text{O}_{19}$	75(10)/13(4)/12(10)	$\text{BaFe}_{9.0(1.2)}^{\text{III}}\text{Fe}_{1.6(5)}^{\text{II}}\text{Ti}_{1.4(8)}^{\text{IV}}\text{O}_{19}$
0.91(7)	69(6)/9(1)/22(6)	$\text{BaFe}_{8.3(7)}^{\text{III}}\text{Fe}_{1.1(1)}^{\text{II}}\text{Ti}_{2.6(7)}^{\text{IV}}\text{O}_{19}$	69(17)/12(5)/19(17)	$\text{BaFe}_{8.3(2.0)}^{\text{III}}\text{Fe}_{1.4(6)}^{\text{II}}\text{Ti}_{2.3(2.0)}^{\text{IV}}\text{O}_{19}$

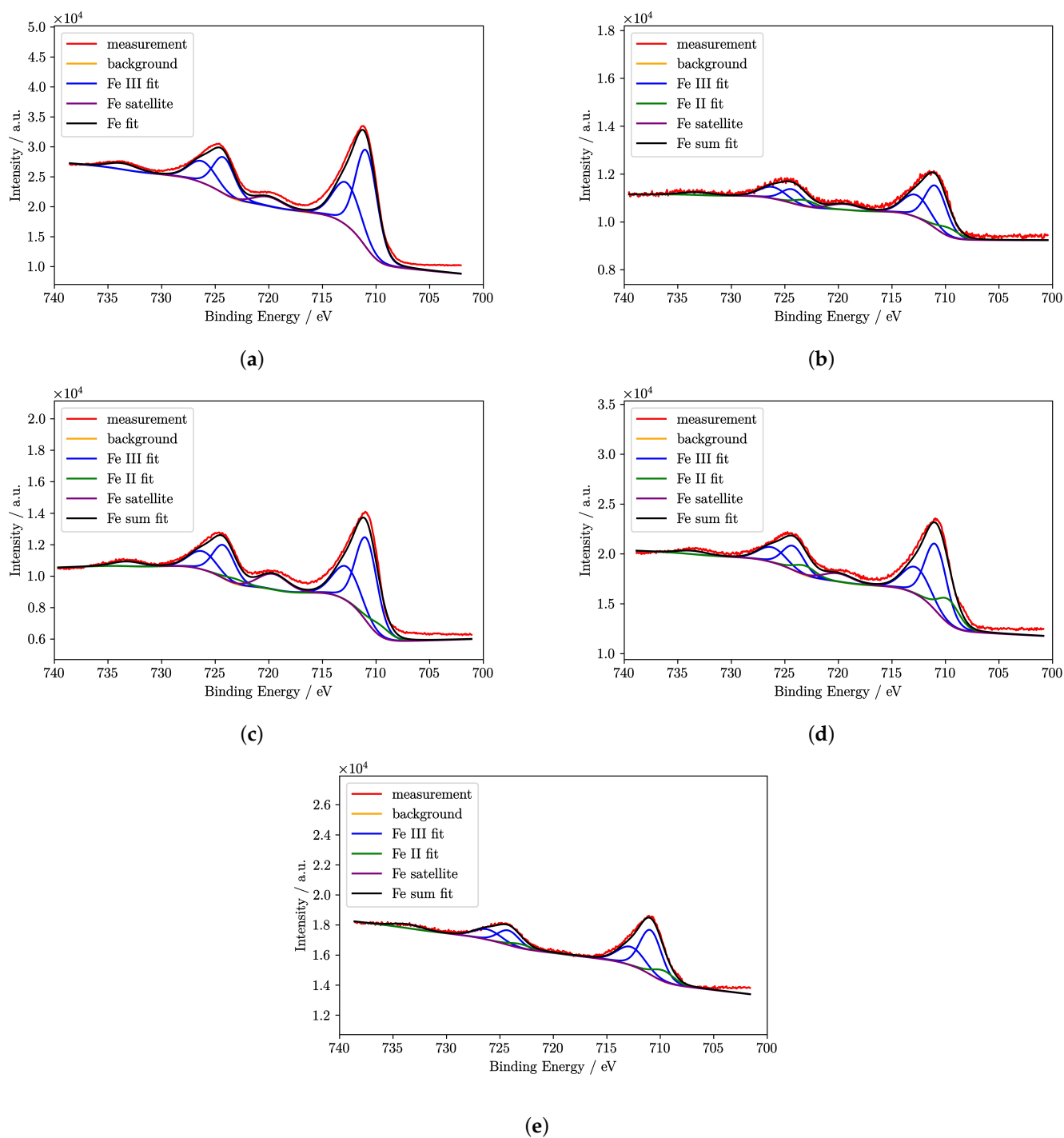


**Figure 11.** XPS Fe 2p spectra of  $\text{BaFe}_{12-x}\text{Ti}_x\text{O}_{19}$  recorded at pass energy 30 eV with (a)  $x = 0$  (2 doublet signals, 1 satellite), (b)  $x = 0.143(5)$  (3 doublet signals, 1 satellite), (c)  $x = 0.49(1)$  (3 doublet signals, 1 satellite), (d)  $x = 0.62(1)$  (3 doublet signals, 1 satellite), (e)  $x = 0.91(7)$  (3 doublet signals, 1 satellite), all including signal deconvolution.

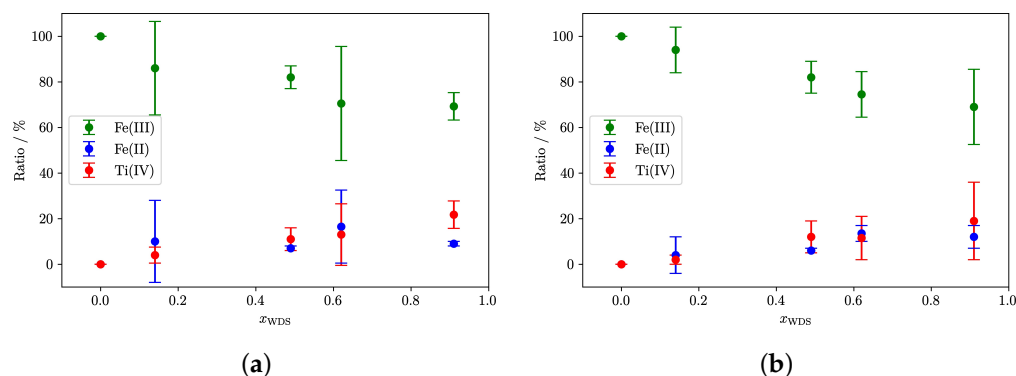


**Figure 12.** Ratios of iron(III) (green)/iron(II) (blue)/titanium(IV) (red) from XPS measurements with (a) pass energy 30 eV (b) pass energy 20 eV.

### 3. Materials and Methods

Black, plate-shaped single crystals with edge lengths up to 1 mm were obtained from sodium carbonate flux. Barium carbonate ( $\text{BaCO}_3$ , Roth, p.a.), iron(III) oxide ( $\text{Fe}_2\text{O}_3$ , Aldrich, 99.99%) and titanium(IV) dioxide ( $\text{TiO}_2$ , Aldrich, >99%) with about 25 mol-% sodium carbonate ( $\text{Na}_2\text{CO}_3$ , Honeywell, p.a.) as flux were homogenized using an agate mortar and heated in a platinum crucible in air up to 1520 K within ten hours. After maintaining the temperature for ten hours, the furnace was cooled down to 870 K within 120 h and then turned off. The ferrimagnetic crude product was separated from the paramagnetic side-products using a permanent magnet and subsequently washed with hot, half-concentrated nitric acid in order to remove residues. The samples were single-phase according to PXRD measurements.

Single crystal X-ray diffraction (SCXRD) was performed using a  $\kappa$ -CCD four circle diffractometer of *Bruker-Nonius* (Karlsruhe, DE) or an IPDS-I single circle diffractometer of *STOE & Cie GmbH* (Darmstadt, DE), both equipped with a graphite monochromator using  $\text{Mo-K}\alpha$  radiation ( $\lambda_{\text{Mo}} = 71.073$  pm). The device used for each measured single crystal is listed in Tables S4–S15 in the Supplementary Materials. For the crystal structure solution and refinements the SHELX-2013 software package was employed [23]. After the measurement the single crystals were washed with liquid paraffin and subsequently with acetone, which evaporated.

Powder X-ray diffraction (PXRD) was carried out using a Stadi P powder diffractometer from *STOE & Cie GmbH* (Darmstadt, DE) equipped with a Mythen 1 K detector from *DECTRIS* (Baden-Daettwil, CH) and  $\text{Mo-K}\alpha$  radiation. For preparation, the sample was ground, fixated on a non-diffracting tape and placed in a flat-bed sample holder. The measurements were carried out in transmission geometry. The unit cell parameters were derived from the diffractograms via the Le Bail profile fitting method [38,39].

Scanning electron microscopy (SEM) and energy and wavelength dispersive X-ray spectroscopy (WDS) were carried out with a *Cameca SX 100* (Gennevilliers Cedex, FR). To avoid an accumulation of charge, the samples were coated with a thin layer of carbon prior to analysis. For quantification standards the minerals barite ( $\text{BaSO}_4$ ), benitoite ( $\text{BaTi}[\text{Si}_3\text{O}_9]$ ) or barium fluoride ( $\text{BaF}_2$ ) for barium, hematite ( $\text{Fe}_2\text{O}_3$ ) for iron and rutile ( $\text{TiO}_2$ ) or benitoite ( $\text{BaTi}[\text{Si}_3\text{O}_9]$ ) for titanium were used.

X-ray photoelectron spectra were recorded on an ESCALAB Xi+ spectrometer by *FEI Deutschland/ThermoScientific* (Dreieich, DE) with a base pressure of  $2 \times 10^{-10}$  mbar. Monochromatic  $\text{Al-K}\alpha$  radiation ( $E = 1468.74$  eV) with a focal spot of 650  $\mu\text{m}$  was used. The survey spectra were recorded with a pass energy of 100 eV, dwell time of 10 ms and 3 scans; the detail spectra were recorded with 30 eV and additionally with 20 eV for Ti 2p and Fe 2p spectra, a dwell time of 100 ms and 20 scans (Ti 2p: 30 scans). As a regular standard procedure, the energy axis was calibrated using the Ag 3d signal of an ion-etched silver sample as reference. The crystals were cleaned with isopropanol in an ultrasonicator. The dried crystals were placed on a conductive carbon tape on a gold support and mounted

on a standard sample holder. They were investigated without further surface treatment, e.g., by ion etching, to avoid the reducing effect of preferential sputtering of light elements, which would alter the oxidation states of transition-metal ions [40]. The spectra were numerically fitted with convoluted Gaussian and Lorentzian profiles using Unifit 2016 [41].

#### 4. Conclusions

M-type barium hexaferrite substituted with various amounts of titanium,  $\text{BaFe}_{12-x}\text{Ti}_x\text{O}_{19}$  with  $0 \leq x < 1.0$ , was synthesized from sodium carbonate flux. Single crystals were selected and characterized with WDS, SCXRD and XPS. Additionally, PXRD measurements were carried out and analyzed using Le Bail refinements for determining trends in the cell parameters  $a$  and  $c$ .

Although WDS is a rather surface-sensitive method, the compositional data from this technique appear most reliable for substituted hexaferrite crystals. A quantitative surface scan indicates a rather homogeneous element distribution within individual crystals, although crystals from one synthesis experiment may have different compositions. The ratio of barium to the sum of the iron and titanium content in the formula reveals the presence of a small but significant vacancy concentration in titanium-substituted barium hexaferrite, which rises with an increasing titanium concentration.

SCXRD is able to indicate the location of titanium and vacancies on the five possible transition-metal sites, but it cannot discriminate between both. Thus, the presence of vacancies observed in WDS mimics a higher degree of substitution by titanium.

XPS univocally shows the presence of iron(II) next to titanium(IV) to a similar extent in substituted crystals. No indication for reduced titanium ions, i.e., titanium(III), were obtained.

The trend for the unit cell size concluding from the PXRD results reveals that at lower degrees of substitution ( $x < 0.3$ ) of iron(III) with titanium(IV) it is foremost charge-compensated by the reduction of iron(III) to iron(II) expressed in an increase in the cell parameters. At higher degrees of substitution, this effect is hidden by the increasing formation of vacancies superimposing a trend toward smaller unit cell parameters, eventually resulting in rather constant cell dimensions essentially independent from  $x$ .

Taking all the results together, we boldly can state that the maximum substitution degree in  $\text{BaFe}_{12-x}\text{Ti}_x\text{O}_{19}$  is close to  $x = 0.9$  for the given synthetic parameters. For the whole range of substitution a major charge balance for this aliovalent substitution system is managed by the reduction of iron(III) to iron(II). However, with an increasing degree of substitution the formation of vacancies as a second mechanism to compensate for the +4 charge of titanium ions becomes more important. Titanium and vacancies seem to predominantly substitute at sites  $M(3)$ ,  $M(4)$  and  $M(5)$  with tetrahedral and two-times octahedral coordination, respectively, while pairs at  $M(4)$  located in face-sharing octahedra are particularly prone to host combinations of titanium(IV) and either iron(II) or a vacancy.

**Supplementary Materials:** The following supporting information can be downloaded at: <https://www.mdpi.com/article/10.3390/inorganics11050207/s1>, Figures S1–S9: SEM patterns. Figures S10–S21: PXRD patterns with Le Bail refinements. Figures S22–S105: XPS spectra. Tables S1–S3: WDS data for all discussed single crystals. Tables S4–S15: Crystallographic data for  $\text{BaFe}_{12}\text{O}_{19}$ ,  $\text{BaFe}_{11.1(2)}\text{Ti}_{0.65(3)}\square_{0.25}\text{O}_{19}$ ,  $\text{BaFe}_{10.7(2)}\text{Ti}_{0.91(7)}\square_{0.36}\text{O}_{19}$ , and  $\text{BaFe}_{11.2(2)}\text{Ti}_{0.61(3)}\square_{0.24}\text{O}_{19}$ . Tables S16–S21: Ratios of Fe(III)/Fe(II), Fe(II)/Ti(IV), and Fe(III)/Fe(II)/Ti(IV) determined with XPS.

**Author Contributions:** Conceptualization, R.N., K.-I.M. and Y.M.D.; validation, R.N. and I.B.; formal analysis, I.B., Y.M.D. and M.H.; investigation, K.-I.M. and M.H.; resources, R.N. and I.B.; data curation, R.N. and I.B.; writing—original draft preparation, K.-I.M.; writing—review and editing, M.H., Y.M.D., I.B. and R.N.; visualization, K.-I.M. and M.H.; supervision, R.N. and I.B.; project administration, R.N.; funding acquisition, R.N. All authors have read and agreed to the published version of the manuscript.

**Funding:** This research received no external funding.

**Acknowledgments:** We thank Falk Lissner for the SCXRD measurements and Felix Goerigk for support with the WDS.

**Conflicts of Interest:** The authors declare no conflict of interest.

### Abbreviations

The following abbreviations are used in this manuscript:

a.u.	arbitrary unit
p.a.	pro analysi, for analytical purpose
BE	binding energy
EDS	energy dispersive X-ray spectroscopy
SEM	scanning electron microscope
WDS	wavelength dispersive X-ray spectroscopy
XPS	X-ray photoelectron spectroscopy
PXRD	powder X-ray diffraction
SCXRD	single crystal X-ray diffraction

### References

1. Pullar, R.C. Hexagonal ferrites: A review of the synthesis, properties and applications of hexaferrite ceramics. *Prog. Mater. Sci.* **2012**, *57*, 1191–1334. [[CrossRef](#)]
2. Shakirzianov, F.N.; Han, B.; Kiaisec, A.A.; Cheparin, V.P. The effect of nanotubes on electromagnetic waves absorption in composite radioabsorbing materials on the basis of hexagonal ferrites. In Proceedings of the 2009 IEEE 9th International Conference on the Properties and Applications of Dielectric Materials, Harbin, China, 19–23 July 2009; pp. 1211–1214.
3. Morisako, A.; Matsumoto, M.; Naoe, M. Ba-ferrite thin film rigid disk for high density perpendicular magnetic recording. *IEEE Trans. Magn.* **1986**, *22*, 1146–1148. [[CrossRef](#)]
4. Adelsköld, V. X-ray Studies on Magneto-Plumbite,  $Pb_{0.6}Fe_2O_3$ , and other Substances resembling “Beta-Alumina”,  $Na_2O \cdot 11 Al_2O_3$ . *Ark. Kemi Miner. Geol.* **1938**, *12A*, 1–9.
5. Obradors, X.; Collomb, A.; Pernet, M.; Samaras, D.; Joubert, J. C. X-ray analysis of the structural and dynamic properties of  $BaFe_{12}O_{19}$  hexagonal ferrite at room temperature. *J. Solid State Chem.* **1985**, *56*, 171–181. [[CrossRef](#)]
6. Braun, P.B. The crystal structures of a new group of ferromagnetic compounds. *Philips Res. Rep.* **1957**, *12*, 491–548.
7. Häßner, M.; Vinnik, D.A.; Niewa, R. Structure and magnetic properties of a new hexaferrite  $(Ba,Pb)(Fe,Ti)_9O_{15}$ . *Ceram. Int.* **2021**, *47*, 5341–5346. [[CrossRef](#)]
8. Vinnik, D.A.; Zherebtsov, D.A.; Mashkovtseva, L.S.; Nemrava, S.; Bischoff, M.; Perov, N.S.; Semisalova, A.S.; Krivtsov, I.V.; Isaenko, L.I.; Mikhailov, G.G.; et al. Growth, structural and magnetic characterization of Al-substituted barium hexaferrite single crystals. *J. Alloys Compd.* **2014**, *615*, 1043–1046. [[CrossRef](#)]
9. Quiroz, P.; Halbedel, B.; Bustamante, A.; González, J.C. Effect of titanium ion substitution in the barium hexaferrite studied by Mössbauer spectroscopy and X-ray diffraction. *Hyperfine Interact.* **2011**, *202*, 97–106. [[CrossRef](#)]
10. Gudkov, V.V.; Sarychev, M.N.; Zherlitsyn, S.; Zhevstovskikh, I.V.; Averkiev, N.S.; Vinnik, D.A.; Gudkova, S.A.; Niewa, R.; Dressel, M.; Alyabyeva, L.N.; et al. Sub-lattice of Jahn-Teller centers in hexaferrite crystal. *Sci. Rep.* **2020**, *10*, 7076–7091. [[CrossRef](#)]
11. Mariño-Castellanos, P.A.; Moreno-Borges, A.C.; Orozco-Melgar, G.; García, J.A.; Govea-Alcaide, E. Structural and magnetic study of the  $Ti^{4+}$ -doped barium hexaferrite ceramic samples: Theoretical and experimental results. *Physica B* **2011**, *406*, 3130–3136. [[CrossRef](#)]
12. Vinnik, D.A.; Zhivulin, V.E.; Starikov, A.Y.; Gudkova, S.A.; Trofimov, E.A.; Trukhanov, A.V.; Trukhanov, S.V.; Turchenko, V.A.; Matveev, V.V.; Lahderanta, E.; et al. Influence of titanium substitution on structure, magnetic and electric properties of barium hexaferrites  $BaFe_{12-x}Ti_xO_{19}$ . *J. Magn. Magn. Mater.* **2020**, *498*, 166117. [[CrossRef](#)]
13. Vinnik, D.A.; Zhivulin, V.E.; Uchaev, D.A.; Gudkova, S.A.; Zhivulin, D.E.; Starikov, A.Y.; Trukhanov, S.V.; Turchenko, V.A.; Zubar, T.I.; Gavrilova, T.P.; et al. Effect of titanium substitution and temperature variation on structure and magnetic state of barium hexaferrites. *J. Alloys Compd.* **2021**, *859*, 158365. [[CrossRef](#)]
14. Vinnik, D.A.; Starikov, A.Y.; Zhivulin, V.E.; Astapovich, K.A.; Turchenko, V.A.; Zubar, T.I.; Trukhanov, S.V.; Kohout, J.; Kmječ, T.; Yakovenko, O.; et al. Structure and magnetodielectric properties of titanium substituted barium hexaferrites. *Ceram. Int.* **2021**, *47*, 17293. [[CrossRef](#)]
15. Vinnik, D.A.; Starikov, A.Y.; Zhivulin, V.E.; Astapovich, K.A.; Turchenko, V.A.; Zubar, T.I.; Trukhanov, S.V.; Kohout, J.; Kmječ, T.; Yakovenko, O.; et al. Changes in the Structure, Magnetization, and Resistivity of  $BaFe_{12-x}Ti_xO_{19}$ . *ACS Appl. Electron. Mater.* **2021**, *3*, 1583. [[CrossRef](#)]
16. Trukhanov, S.V.; Zubar, T.I.; Turchenko, V.A.; Trukhanov, A.V.; Kmječ, T.; Kohout, J.; Matzui, L.; Yakovenko, O.; Vinnik, D.A.; Starikov, A.Y.; et al. Exploration of crystal structure, magnetic and dielectric properties of titanium-barium hexaferrites. *Mater. Sci. Eng.* **2021**, *B272*, 115345. [[CrossRef](#)]
17. Nemrava, S.; Vinnik, D.A.; Hu, Z.; Valldor, M.; Kuo, C.-Y.; Zherebtsov, D.A.; Gudkova, S.A.; Chen, C.-T.; Tjeng, L.H.; Niewa, R. Three oxidation states of manganese in the barium hexaferrite  $BaFe_{12-x}Mn_xO_{19}$ . *Inorg. Chem.* **2017**, *56*, 3861–3866. [[CrossRef](#)] [[PubMed](#)]

18. Nemrava, S. Synthese und Charakterisierung iso- und aliovalent substituierter M-artiger Ferrite und Ferrite des R-Typs. Doctoral Dissertation, University of Stuttgart, Stuttgart, Germany, 2017.
19. Siegrist, T.; Vanderah, T.A. Combining magnets and dielectrics: Crystal chemistry in the BaO-Fe<sub>2</sub>O<sub>3</sub>-TiO<sub>2</sub> system. *Eur. J. Inorg. Chem.* **2003**, *8*, 1483–1501. [[CrossRef](#)]
20. Townes, W.D.; Fang, J.H.; Perrotta, A.J. The crystal structure and refinement of ferrimagnetic barium ferrite, BaFe<sub>12</sub>O<sub>19</sub>. *Z. Kristallogr.* **1967**, *125*, 437–449. [[CrossRef](#)]
21. Holleman, A.F.; Wiberg, E.; Wiberg, N.; Fischer, G. *Anorganische Chemie, Band 2: Nebengruppenelemente, Lanthanoide, Actinoide, Transactinoide*, 103th ed.; de Gruyter: Berlin, Germany, 2017.
22. Sheldrick, G.M. A short history of SHELX. *Acta Crystallogr.* **2008**, *A64*, 112–122. [[CrossRef](#)]
23. Sheldrick, G.M. Crystal structure refinement with SHELXL. *Acta Crystallogr.* **2015**, *C71*, 3–8.
24. Pauling, L. The principles determining the structure of complex ionic crystals. *J. Am. Chem. Soc.* **1929**, *51*, 1010–1026. [[CrossRef](#)]
25. Ohgaki, K.; Ohgaki, M.; Tanaka, K.; Marumo, F.; Takei, K. Electron-density distribution in ilmenite-type crystals, IV. Iron (II) titanium (IV) trioxide, FeTiO<sub>3</sub>. *Miner. J.* **1989**, *14*, 179–190. [[CrossRef](#)]
26. Müller, U. *Anorganische Strukturchemie*, 6th ed.; Vieweg + Teubner: Wiesbaden, Germany, 2008.
27. Shannon, R.D.; Prewitt, C.T. Effective Ionic Radii in Oxides and Fluorides. *Acta Crystallogr.* **1969**, *B25*, 925–946. [[CrossRef](#)]
28. Moulder, J.F.; Stickle, W.F.; Sobol, P.E.; Bomben, K.D. *Handbook of X-ray Photoelectron Spectroscopy*, 1st ed.; Perkin-Elmer Corporation: Eden Prairie, MN, USA, 1992.
29. Hashimoto, S.; Tanaka, A. Alteration of Ti 2p XPS spectrum for titanium oxide by low-energy Ar ion bombardment. *Surf. Interface Anal.* **2002**, *34*, 262–265. [[CrossRef](#)]
30. Atuchin, V.V.; Vinnik, D.A.; Gavrilova, T.A.; Gudkova, S.A.; Isaenko, L.I.; Jiang, X.; Pokrovsky, L.D.; Prosvirin, I.P.; Mashkovtseva, L.S.; Lin, Z. Flux Crystal Growth and the Electronic Structure of BaFe<sub>12</sub>O<sub>19</sub> Hexaferrite. *J. Phys. Chem. C* **2016**, *120*, 5114–5123. [[CrossRef](#)]
31. Schmitz, P.J. Characterization of the Surface of BaCO<sub>3</sub> Powder by XPS. *Surf. Sci. Spectra* **2001**, *8*, 190–194. [[CrossRef](#)]
32. López, M.d.C.B.; Fourlaris, G.; Rand, B.; Riley, F.L. Characterization of barium titanate powders: Barium carbonate identification. *J. Am. Ceram. Soc.* **1999**, *82*, 1777–1786. [[CrossRef](#)]
33. Barr, T.L. An XPS study of Si as it occurs in adsorbents, catalysts, and thin films. *Appl. Surf. Sci.* **1983**, *15*, 1–35. [[CrossRef](#)]
34. Biesinger, M.C.; Payne, B.P.; Grosvenor, A.P.; Lau, L.W.; Gerson, A.R.; Smart, R.S. Resolving surface chemical states in XPS analysis of first row transition metals, oxides and hydroxides: Cr, Mn, Fe, Co and Ni. *Appl. Surf. Sci.* **2011**, *257*, 2717–2730. [[CrossRef](#)]
35. Vasquez, R.P.; Foote, M.C.; Hunt, B.D. Reaction of nonaqueous halogen solutions with YBa<sub>2</sub>Cu<sub>3</sub>O<sub>7-x</sub>. *Surf. Interface Anal.* **1989**, *66*, 4866–4877. [[CrossRef](#)]
36. Yeh, J.J.; Lindau, I. Atomic subshell photoionization cross sections and asymmetry parameters: 1 ≤ Z ≤ 103. *At. Data Nucl. Data Tables* **1985**, *32*, 1–155. [[CrossRef](#)]
37. Thermo Fisher Scientific. Thermo Advantage (v5.9925), 1999–2021. Available online: <https://www.thermofisher.cn/cn/en/home.html> (accessed on 22 March 2023).
38. Le Bail, A. Whole powder pattern decomposition methods and applications: A retrospection. *Powder Diffr.* **2005**, *20*, 316–326. [[CrossRef](#)]
39. Le Bail, A.; Duroy, H.; Fourquet, J.L. Ab-initio structure determination of LiSbWO<sub>6</sub> by X-ray powder diffraction. *Mater. Res. Bull.* **1988**, *23*, 447–452. [[CrossRef](#)]
40. Behrisch, R.; Eckstein, W. Sputtering by particle bombardment, Experiments and Computer Calculations from Threshold the MeV energies. In *Topics in Applied Physics—Volume 110*; Springer: Berlin, Germany, 2007.
41. Hesse, R.; Chassé, T.; Szargan, R. Peak shape analysis of core level photoelectron spectra using UNIFIT for WINDOWS. *Fresenius J. Anal. Chem.* **1999**, *365*, 48–54. [[CrossRef](#)]

**Disclaimer/Publisher’s Note:** The statements, opinions and data contained in all publications are solely those of the individual author(s) and contributor(s) and not of MDPI and/or the editor(s). MDPI and/or the editor(s) disclaim responsibility for any injury to people or property resulting from any ideas, methods, instructions or products referred to in the content.